

Effect of mechanical strain on the optical properties of nodal-line semimetal ZrSiS

Weiying Zhou,¹ A. N. Rudenko,^{1,2,3,*} and Shengjun Yuan^{1,†}

¹*Key Laboratory of Artificial Micro- and Nano-structures of Ministry of Education and School of Physics and Technology, Wuhan University, Wuhan 430072, China*

²*Institute for Molecules and Materials, Radboud University, Heijendaalseweg 135, NL-6525 AJ Nijmegen, The Netherlands*

³*Theoretical Physics and Applied Mathematics Department, Ural Federal University, 620002 Ekaterinburg, Russia*

(Dated: June 16, 2022)

Optical properties of nodal-line semimetal ZrSiS are studied using first-principles calculations. Frequency-independent optical conductivity is a fingerprint of the infrared optical response in ZrSiS. We find that this characteristic feature is robust with respect to external pressure of up to 10 GPa, yet with the flat region being narrowed with increasing pressure. Upon tensile stress of 2 GPa, the Fermi surface undergoes a topological transition accompanied by a weakening of the interband screening, which reduces the spectral weight of infrared excitations. We also show that the high-energy region is characterized by low-loss plasma excitations at ~ 20 eV with essentially anisotropic dispersion. Strongly anisotropic dielectric properties suggest the existence of a hyperbolic regime for plasmons in the deep ultraviolet range. Although the frequencies of high-energy plasmons are virtually unaffected by external pressure, their dispersion can be effectively tuned by strain.

I. INTRODUCTION

As three-dimensional analogues of graphene, Dirac and Weyl semimetals have attracted considerable attention in the last years [1–5]. Both Dirac and Weyl materials are characterized by linearly dispersing valence and conduction bands that cross at discrete point in momentum space, giving rise to low-energy excitations behaving like Dirac or Weyl fermions. Recently, a novel class of topological materials, nodal-line materials, has been predicted [6, 7]. In comparison to Dirac and Weyl semimetals, band crossing in nodal-line semimetals occurs along continuous lines. Since 2011, several materials were proposed to be nodal-line semimetals [8–10], and some of them have been confirmed experimentally using such techniques as angle-resolved photoemission spectroscopy (ARPES) [11–13] and magnetotransport measurements [14–16].

The family of ternary compounds ZrSiX ($X=\text{S, Se, Te}$) is a typical example of nodal-line semimetal with well separated Dirac cones [12, 17]. The presence of topologically nontrivial linear bands in ZrSiX has been observed experimentally by several methods, including ARPES [12, 18–20], scanning probe techniques [21, 22], as well as thermoelectric [15] and magnetotransport [23–28] measurements of quantum oscillations. Among ZrSiX s, ZrSiS is especially prospective material for optoelectronic applications due to its high carrier mobility [15, 29], thermal stability [30], and non-toxic nature [31]. A significant attention has been paid to ZrSiS due to its unusual properties observed in experiment. Particularly, ARPES experiments reveal that ZrSiS hosts two kinds of nodal lines. While in the first kind the degeneracy of Dirac points is protected by non-symmorphic symmetry, in the second kind the degeneracy is lifted by the spin-orbit coupling, inducing a small gap of the order of 10 meV [12]. The upper limit of this gap (~ 30 meV) is observed by recent low-frequency

optical measurements [32]. Compared to other known 3D Dirac materials, the energy range of the linearly dispersing bands in ZrSiS reaches 2 eV, making this material a promising candidate for studying Dirac fermions. Apart from Dirac physics, extremely strong Zeeman splitting with a large g -factor has been observed by measuring de Haas-van Alphen (dHvA) oscillations [24]. There is also evidence of an important role of the correlation effects in ZrSiS and related materials. The unusual mass enhancement of charge carriers in ZrSiS has been recently observed experimentally at low-temperatures [23], which can be understood in terms of unconventional electron-hole pairing [33, 34]. Last but not least, recent high-pressure electrical transport measurements pointed to the possibility of a topological phase transition in ZrSiS below 0.5 GPa [35].

Recently, optical spectra of ZrSiS were measured in a large frequency range, from the near-infrared to the visible [32]. It was found that the absorption spectrum remain almost unchanged for photon energies in the range from 30 meV to 350 meV [32]. The flat optical conductivity is typical for graphene and graphite, being a universal constant for Dirac electrons in two dimensions [36, 37]. In three dimensions, this behavior is not universal, whereas the flatness of the optical conductivity in ZrSiS is determined by an appropriate combination of intraband and interband transitions [38]. Followed by the flat region, the optical conductivity in ZrSiS exhibits a characteristic U-shape ending at a sharp peak around 1.3 eV [32, 39]. Interestingly, the optical response is strongly anisotropic with the 1.3 eV peak appearing in the in-plane [100] direction only [38]. Besides, essentially anisotropic magnetoresistance in ZrSiS has been measured experimentally [25, 40]. Recent findings on the family of compounds ZrSiX ($X=\text{S, Se, Te}$) and ZrGeX ($X=\text{S, Te}$) suggest that their optical properties are closely connected to the interlayer bonding, and can be tuned by external pressure [39].

Unlike infrared and visible spectral regions, ultraviolet optical response of ZrSiS has not been studied yet.

* a.rudenko@science.ru.nl

† s.yuan@whu.edu.cn

Besides that, previous works focus on the optical properties of pristine ZrSiS, while effect of strain, has not been addressed in detail. The ultraviolet region is especially appealing for plasmonic applications, for which ZrSiS appears promising due to its high carrier mobility, closely related to the sustainability of plasmonic modes. Short propagation length (lifetime) of plasmons in typical plasmonic materials (e.g., noble metals) represents a bottleneck for applications [41]. At the same time, the application domain of ultraviolet plasmonics is highly diverse. It includes biochemical sensing applications [42, 43], photodetection [44], nano-imaging [45], material characterization [46], and absorption of radiation [47].

In this paper, we study broadband optical properties of ZrSiS crystals with a special emphasis on the effect of external strain. To this end, we use first-principles calculations in combination with the random phase approximation for the dielectric screening. We find that although the low-energy optical conductivity remains frequency-independent under external pressure of up to 10 GPa, the corresponding spectral region is narrowing with increasing pressure. In the presence of tension, we observe an electronic topological transition at around 2 GPa. This transition results in a suppressed intraband screening, which reduces the spectral weight in the infrared region. Apart from the flat optical conductivity at low energies, our calculations show that ZrSiS is characterized by high-energy plasma excitations with frequencies around 20 eV. Given that the optical response in ZrSiS is highly anisotropic, it permits the existence of low-loss hyperbolic plasmons in the ultraviolet spectral range.

The paper is organized as follows. In Sec. II, we describe our computational method and calculation details. Optical properties of pristine ZrSiS are presented in Sec. III, where we specifically focus on the low- and high-energy spectral regions. In Sec. IV, we study the effect of external strain on the optical conductivity and plasma excitations in ZrSiS. In Sec. V, we summarize our findings.

II. CALCULATION DETAILS

A. Electronic structure

ZrSiS is a layered crystal with a tetragonal structure and space group $P4/nmm$ (No.129). Its structure is formed by Zr-S layers sandwiched between Si layers, and periodically repeated in the direction normal to the layers, as shown in Figure. 1(a). The equilibrium lattice constants obtained from full structural optimization at the DFT level are $a = 3.56$ Å (in-plane) and $c = 8.17$ Å (out-of-plane). The DFT electronic structure calculations are performed within the pseudopotential plane-wave method as implemented in QUANTUM ESPRESSO [48] simulation package. We use generalized gradient approximation (GGA) [49] in combination with norm-conserving pseudopotentials [50], in which 4s and 4d electrons of Zr, 3s and 3p electrons of Si, as well as 3s and 3p electrons

of S were treated as valent. The reciprocal space was sampled by a uniform $(24 \times 24 \times 8)$ \mathbf{k} -point mesh. In the calculations, we set the energy cutoff for the plane-wave basis to 80 Ry, and a self-consistency threshold for the total energy to 10^{-12} Ry. The atomic structure and lattice parameters were optimized until the residual forces on each atom were less than 10^{-5} Ry/Bohr. The effect of spin-orbit coupling is not taken into account in our study as it is only relevant for low temperatures (< 100 K) and in the low-frequency region (< 20 meV) [32]. All crystal graphics was generated by means of XCrySDen visualization package [51].

B. Dielectric function

Dielectric function $\epsilon(\mathbf{q}, \omega)$ was calculated within the random phase approximation (RPA) using YAMBO [52] package. Its standard form as function of wave vector \mathbf{q} and frequency of incident photon ω reads:

$$\epsilon(\mathbf{q}, \omega) = 1 - v(\mathbf{q})\chi^0(\mathbf{q}, \omega), \quad (1)$$

where $v(\mathbf{q}) = \frac{4\pi e^2}{|\mathbf{q}|^2}$ is the bare Coulomb potential, χ^0 is the irreducible response function evaluated within the independent particle approximation [52]:

$$\chi^0(\mathbf{q}, \omega) = \frac{2}{V} \sum_{\mathbf{k}, nm} \rho_{nm\mathbf{k}}^*(\mathbf{q}) \rho_{nm\mathbf{k}}(\mathbf{q}) \times \left[\frac{f_{n\mathbf{k}-\mathbf{q}}(1 - f_{m\mathbf{k}})}{\omega + \varepsilon_{n\mathbf{k}-\mathbf{q}} - \varepsilon_{m\mathbf{k}} + i\eta} - \frac{f_{n\mathbf{k}}(1 - f_{m\mathbf{k}-\mathbf{q}})}{\omega + \varepsilon_{m\mathbf{k}} - \varepsilon_{n\mathbf{k}-\mathbf{q}} - i\eta} \right], \quad (2)$$

where

$$\rho_{nm\mathbf{k}}(\mathbf{q}) = \langle n\mathbf{k} | e^{i\mathbf{q} \cdot \mathbf{r}} | m\mathbf{k} - \mathbf{q} \rangle \quad (3)$$

is the dipole transition matrix element, $f_{n\mathbf{k}}$ is the Fermi occupation factor, for which $T = 300$ K was used in all calculations, $|n\mathbf{k}\rangle$ is the Bloch eigenstate corresponding to the band n and wave vector \mathbf{k} , and V is the cell volume. To avoid computationally demanding calculations, we assume the scalar form of $\epsilon(\mathbf{q}, \omega)$ and $\chi^0(\mathbf{q}, \omega)$, meaning that only $\mathbf{G} = 0$ and $\mathbf{G}' = 0$ elements of the full matrices are calculated. Physically, this approximation corresponds to the situation, in which the local field effects are neglected, i.e. $\epsilon(\mathbf{r}_1, \mathbf{r}_2) \simeq \epsilon(|\mathbf{r}_1 - \mathbf{r}_2|)$. This approximation is well justified for 3D systems with weak inhomogeneities of the charge density [53]. In Eq. (2), η is the damping parameter playing the role of the electron linewidth, which can be attributed to the imaginary part of the self-energy, $\eta \sim \text{Im}[\Sigma(\omega, \mathbf{k})]$ [54]. Here, we do not detail the scattering mechanism and consider η as a free parameter.

To reproduce the quantities measured in optical experiments, one needs to evaluate the long-wavelength limit of the dielectric function,

$$\epsilon_{\alpha\alpha}(\omega) \equiv \lim_{\mathbf{q} \rightarrow 0} \epsilon(\mathbf{q}, \omega), \quad (4)$$

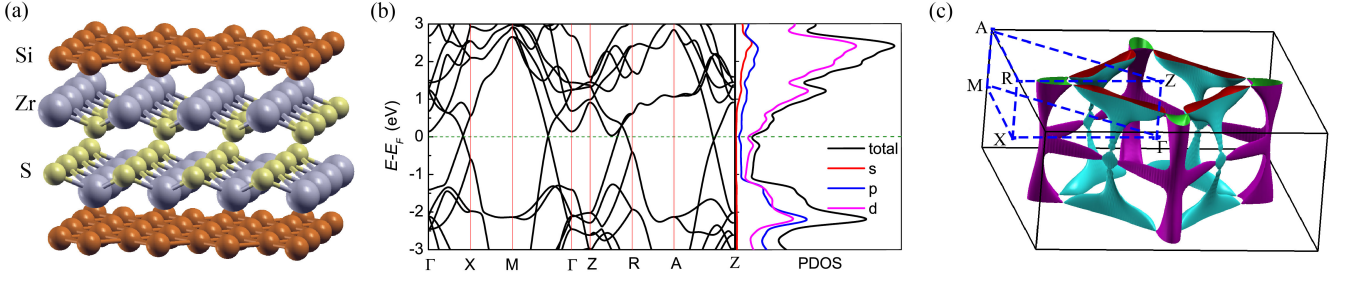


FIG. 1. (a) Schematic representation of the ZrSiS crystal structure; (b) Calculated band structure and orbital-resolved density of states in the vicinity of the Fermi energy; (c) Three-dimensional view of the Fermi surface with purple and cyan colors denoting valence and conduction states, respectively. Black lines mark the Brillouin zone boundaries. Dashed blue lines connect the high-symmetry points used in (b).

where α is the direction of the incident light, and the limit is taken with \mathbf{q} parallel to α . Taking this limit numerically is a computationally nontrivial task as it requires high density of \mathbf{q} -point to be included in the calculations. This can be avoided by expanding the dipole transition matrix elements at $\mathbf{q} \rightarrow 0$ using $e^{i\mathbf{q}\cdot\mathbf{r}} \approx 1 + i\mathbf{q}\cdot\mathbf{r}$. To this end, the matrix elements $\mathbf{r}_{nm\mathbf{k}} = \langle n\mathbf{k}|\mathbf{r}|m\mathbf{k} \rangle$ needs to be computed. Within the periodic boundary conditions using the relation $[\mathbf{r}, H] = \mathbf{p} + [\mathbf{r}, V_{nl}]$ one arrives at [55]

$$\langle n\mathbf{k}|\mathbf{r}|m\mathbf{k} \rangle = \frac{\langle n\mathbf{k}|\mathbf{p} + [\mathbf{r}, V_{nl}]|m\mathbf{k} \rangle}{\varepsilon_{n\mathbf{k}} - \varepsilon_{m\mathbf{k}}} \quad (5)$$

where V_{nl} is the nonlocal part of the pseudopotential.

At $\mathbf{q} \rightarrow 0$, Eq. (2) does not explicitly takes intraband transitions into account. Since ZrSiS is a semimetal, the intraband transition provide an important contribution to the dielectric response at low energies. To account for this contribution, we calculate the Drude corrections to the dielectric function $\epsilon_{\alpha\alpha}^{\text{intra}}(\omega) = \epsilon_{1,\alpha\alpha}^{\text{intra}}(\omega) + i\epsilon_{2,\alpha\alpha}^{\text{intra}}(\omega)$, which are evaluated from the standard free-electron plasma model [56]:

$$\begin{aligned} \epsilon_{1,\alpha\alpha}^{\text{intra}}(\omega) &= 1 - \frac{\omega_{p,\alpha\alpha}^2}{\omega^2 + \delta^2}, \\ \epsilon_{2,\alpha\alpha}^{\text{intra}}(\omega) &= \frac{\delta\omega_{p,\alpha\alpha}^2}{\omega^3 + \omega\delta^2}. \end{aligned} \quad (6)$$

Here, δ has similar physical meaning as η in Eq. (2), and $\omega_{p,\alpha\alpha}$ is the α -component of the (unscreened) plasma frequency given by [57, 58]:

$$\omega_{p,\alpha\beta}^2 = -\frac{4\pi e^2}{V} \sum_{n,\mathbf{k}} \frac{\partial f_{n\mathbf{k}}}{\partial \varepsilon_{n\mathbf{k}}} v_{n\mathbf{k}}^\alpha v_{n\mathbf{k}}^\beta \quad (7)$$

where $v_{n\mathbf{k}}^\alpha = \hbar^{-1} \partial \varepsilon_{n\mathbf{k}} / \partial k_\alpha$ is the α -component of the group velocity of the electrons with wave vector \mathbf{k} at band n . In this work, the plasma frequency is calculated using the SIMPLE code [59].

The intraband contribution to the optical conductivity can be calculated accordingly, using the well-known

expressions [54]:

$$\begin{aligned} \sigma_{1,\alpha\alpha}^{\text{intra}}(\omega) &= \frac{\omega \epsilon_{2,\alpha\alpha}^{\text{intra}}(\omega)}{4\pi} \\ \sigma_{2,\alpha\alpha}^{\text{intra}}(\omega) &= 1 - \frac{\omega \epsilon_{1,\alpha\alpha}^{\text{intra}}(\omega)}{4\pi} \end{aligned} \quad (8)$$

III. OPTICAL PROPERTIES OF PRISTINE ZRSIS

A. Low-energy region

We first calculate the electronic structure of ZrSiS for its equilibrium crystal structure. In Figure. 1, we show the band structure, density of states projected on s -, p -, and d -orbitals (PDOS), and the corresponding Fermi surface. The most prominent feature of the band structure is a series of linearly dispersing bands with the Dirac-like crossings in the vicinity of the Fermi energy (ε_F). The linear bands extend over a rather large energy range of up to 2 eV. From Figure. 1(b), one can see that DOS exhibits a minimum at ε_F , as expected near the band crossing points. In the range from -1 to 0 eV, the valence states are entirely formed by linearly dispersed bands, while the states above ε_F are mixed with quadratic bands, giving rise to a larger DOS for the conduction band. As can be seen from PDOS, d -orbitals have dominant contribution to the states near ε_F . At $\varepsilon \lesssim 1$ eV there is a comparable contribution from p -orbitals. In Figure. 1(c), we show the corresponding Fermi surface. It is composed of two distinct parts, corresponding to electron (cyan) and hole (purple) states. Each part is formed by four disconnected pockets. As we will see below, the Fermi surface topology plays an important role in the optical properties of strained ZrSiS.

After the ground state electronic structure is obtained, we calculate the dielectric functions, and the corresponding optical conductivities. We start from the $\mathbf{q} \rightarrow 0$ limit and first calculate the unscreened plasma frequencies using Eq. (7). We arrive at $\omega_{p,xx} = 3.15$ eV and $\omega_{p,zz} = 1.08$ eV for the in-plane $[100]$ and out-of plane $[001]$ components, respectively. The value obtained for

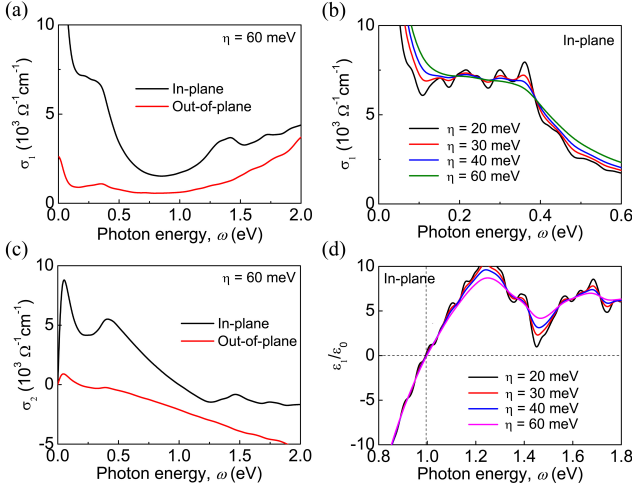


FIG. 2. (a) Real part of the optical conductivity shown as a function of the photon energy with incidence along in-plane [100] and out-of-plane [001] crystallographic directions; (b) Real part of the in-plane optical conductivity calculated for different damping parameters η ; (c) Imaginary part of the optical conductivity calculated along [100] and [001] directions; (d) Real part of the in-plane dielectric function calculated for different η .

the [100] directions is in good agreement with the experimental estimate of 2.88 eV [32]. In Figures. 2(a) and 2(c), we show the real and imaginary parts of the optical conductivity calculated in the region up to 2 eV for [100] and [001] directions of photon propagation. The spectral weight obtained for the in-plane direction is significantly larger compared to the out-of-plane direction. This indicates a strong anisotropy between the optical response in ZrSiS.

In order to assess sensitivity of the optical conductivity to the effects induced by finite electron linewidth, in Figure. 2(b) we show the real part of the low-energy optical conductivity calculated for different parameters η at the range from 20 to 60 meV. From Figure. 2(b), one can clearly see the prominent flat conductivity from 0.1 to 0.4 eV. The flat conductivity σ_{flat} is estimated to be $\sim 7000 \Omega^{-1} \text{cm}^{-1}$, which is good agreement with the experimental result of $6600 \Omega^{-1} \text{cm}^{-1}$ [32]. The flatness is well reproduced for $\eta = 30\text{--}40$ meV, while larger values result in a noticeable smearing of the flat region. For $\eta \lesssim 20$ meV, one can see the emergence of an oscillatory behavior. This behavior is of the numerical origin, and can be associated with insufficient sampling of the Brillouin zone. In what follows, we set $\eta = 40$ meV in all low-energy (0–2 eV) conductivity calculations. This value is in agreement with the electron linewidth experimentally estimated in ZrSiS as ~ 30 meV at 300 K [32]. Following the flat region, there appears a U-shaped optical conductivity around 1.3 eV [39]. The peak above the U-shaped region at ~ 1.3 eV is only found for the in-plane direction, while it is absent in the out-of-plane direction. This peak mainly originates from the excitation between the linearly dispersing bands near ε_F and from the tran-

sitions between quadratic bands in the direction from Z to R.

In Figure. 2(d), we show the real part of the calculated in-plane dielectric function. The condition $\epsilon_1(\omega_p^{\text{scr}}) = 0$ allows us to estimate the screened plasma frequency, which is found to be $\omega_p^{\text{scr}} \sim 1$ eV. Having determined ω_p^{scr} , we can estimate the effective screening induced by the interband transitions [56]. The corresponding dielectric constant $\epsilon_\infty = (\omega_p/\omega_p^{\text{scr}})^2 \approx 9$, which is consistent with the experimental value of ~ 7.8 [32]. To understand the effect of finite electron linewidth on ω_p^{scr} , we also plot $\epsilon_1(\omega)$ for different parameters η in Figure. 2(d). Compared to the flatness of the optical conductivity, the screened plasma frequency is almost insensitive to η .

B. High-energy region

We now turn to the optical response in the high energy region, $\omega > 2$ eV. Here, we focus at the plasmonic excitations and consider momentum-resolved dielectric function $\epsilon(\mathbf{q}, \omega)$, which is shown in Figure. 3 as a function of the photon energy for a series of small wave vectors \mathbf{q} in both in-plane and out-of-plane directions. At $\omega \gtrsim 10$ eV, $\epsilon(\mathbf{q}, \omega)$ is monotonic at small \mathbf{q} , with $\epsilon(\mathbf{q}, \omega) \rightarrow 1$ as $\omega \rightarrow \infty$, which is expected from the Drude model [Eq. (6)]. The most interesting energy region is determined by the condition $\epsilon_1(\mathbf{q}, \omega) = 0$, which defines the existence of plasma excitations. From Figure. 3, one can see that this criterion is fulfilled for two different energy regions: $\omega_p \sim 5\text{--}7$ and $\omega_p \sim 19\text{--}20$ eV. To gain more insights in the plasmonic response, we calculate the energy loss function

$$L(\mathbf{q}, \omega) = -\text{Im} \left[\frac{1}{\epsilon(\mathbf{q}, \omega)} \right], \quad (9)$$

which can be associated with the Electron Energy Loss Spectroscopy (EELS) spectra. Figure. 4 shows $L(\mathbf{q}, \omega)$ calculated along the in-plane and out-of-plane directions of ZrSiS. In both cases, one can see a sharp peak around 20 eV, while there is no indication of the energy loss at lower energies. This means that the plasma oscillations around 5–7 eV are strongly damped. This can be understood from Figure. 3, where $\epsilon_2(\mathbf{q}, \omega)$ exhibits a peak around $\omega \sim 5$ eV, indicating strong absorption in this region. On the other hand, $\epsilon_2(\mathbf{q}, \omega)$ is almost zero around $\omega \sim 20$ eV, indicating that high-energy plasmons are characterized by low losses, and could be observed experimentally. Recently, similar behavior has been experimentally observed in bulk black phosphorus crystal in the same frequency region [60].

The dispersion of bulk plasmons can be fitted with a second-order polynomial:

$$E(\mathbf{q}) = E(0) + A\mathbf{q}^2, \quad (10)$$

where $E(0)$ is the plasmon energy at $\mathbf{q} \rightarrow 0$ and A is the dispersion coefficient. From Figure. 4, it can be seen that the calculated dispersion can indeed be fitted with

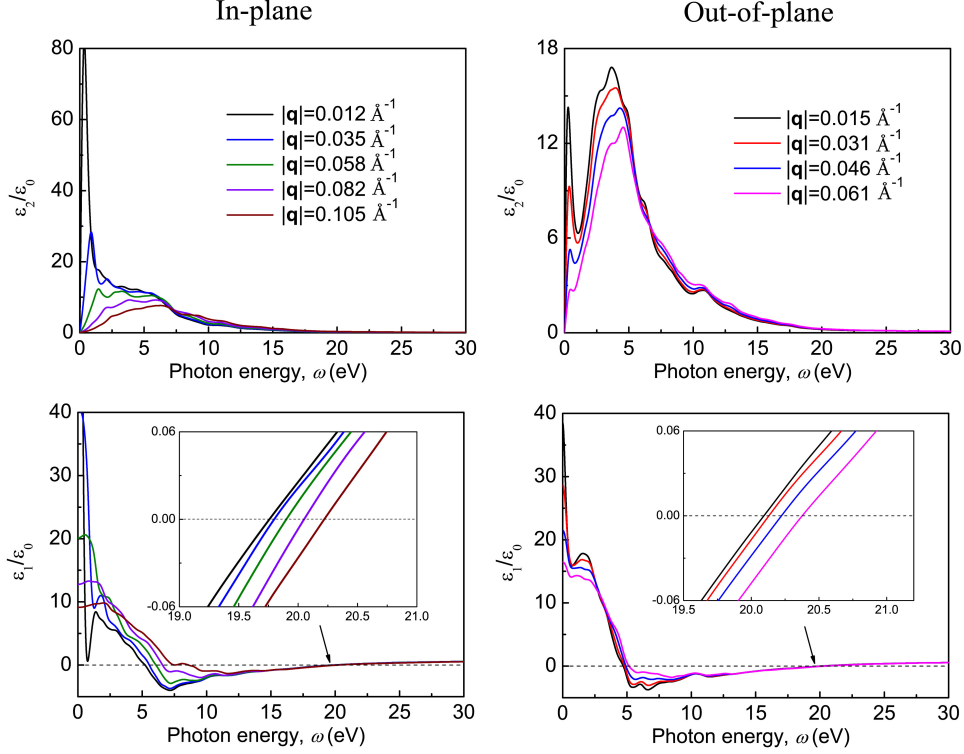


FIG. 3. Imaginary (upper panels) and real (lower panels) parts of the dielectric function of pristine ZrSiS calculated as a function of the photon energy ω for a series of wave vectors \mathbf{q} along the in-plane (left panels) and out-of-plane (right panels) directions. Inset shows a zoom-in of the high-energy region where $\epsilon_1(\mathbf{q}, \omega) = 0$.

Eq. (10). Interestingly, although the plasma frequency is nearly independent of the direction of light propagation, the dispersion of high-energy plasmon modes is strongly anisotropic. The existence of high-energy plasmons in ZrSiS might be beneficial in the context of ultraviolet optical devices [61]. At the same time, strongly anisotropic dispersion of plasmon modes may give rise to unconventional plasma excitations, known as hyperbolic plasmons [62].

Hyperbolic plasmons appear in crystals with strong anisotropy, in which effective permittivity changes sign with respect to the electric field direction [63]. The dispersion relation of light propagating in homogeneous layered material is determined by the relation:

$$\frac{(k_x^2 + k_y^2)}{\epsilon_{zz}(\omega)} + \frac{k_z^2}{\epsilon_{xx}(\omega)} = \frac{\omega^2}{c^2}, \quad (11)$$

where ϵ_{xx} and ϵ_{zz} are the frequency-dependent permittivities along the in-plane and out-of-plane directions, respectively. For frequencies at which $\epsilon_{xx}(\omega) \cdot \epsilon_{zz}(\omega) < 0$, the equation above describes a hyperboloid. This situation is considerably different from the closed spherical or elliptic dispersion typical for conventional materials with $\epsilon_{xx}(\omega) \cdot \epsilon_{zz}(\omega) > 0$ [64, 65]. Depending on the form of the isofrequency surface, one can distinguish between the two types of hyperbolic materials: Type I if the hyperboloid is two-sheeted ($\epsilon_{zz} < 0, \epsilon_{xx} > 0$), and type II if the hyperboloid is single-sheeted ($\epsilon_{zz} > 0, \epsilon_{xx} < 0$).

In Figure. 5(a), we show the corresponding permittivities calculated in ZrSiS as a function of the photon energy. One can see that the condition $\epsilon_{xx}(\omega) \cdot \epsilon_{zz}(\omega) < 0$ is fulfilled in a narrow energy region around ~ 5 eV and ~ 20 eV, which are the frequencies at which the conventional bulk plasmon modes are found. In both cases, the hyperbolic plasmons may appear in a frequency range of about 0.6 eV. Both hyperbolic modes demonstrate the dispersion relation of type I, corresponding to a two-sheeted hyperboloid, shown in Figure. 5(b). Similar to other natural hyperbolic materials, hyperbolic regimes in ZrSiS appear only above the onset of intraband transition [64]. Since electromagnetic waves propagating in hyperbolic materials follow the hyperbolic dispersion, hyperbolic media supports propagation of high- \mathbf{k} waves that are evanescent in conventional media [63]. Due to the properties of high- \mathbf{k} waves, hyperbolic material have many potential applications, including negative refraction [66, 67], sub-wavelength modes [68] and thermal emission engineering [69]. We note, however, since the ~ 5 eV mode is strongly damped, its practical significance is questionable.

IV. OPTICAL PROPERTIES OF STRAINED ZRSIS

Earlier studies on the family of compounds ZrSiX (X=S, Se, Te) suggest that their physical properties are

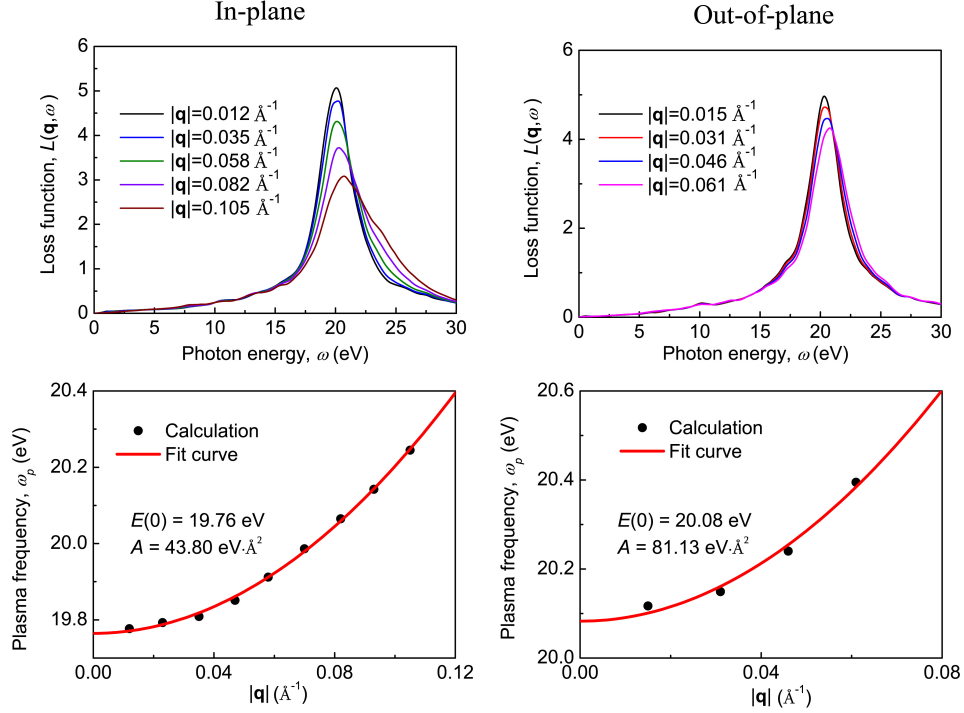


FIG. 4. Upper panels: Electron energy loss spectrum $L(\mathbf{q}, \omega)$ as a function of the photon energy ω and momentum \mathbf{q} calculated for the in-plane (left) and out-of-plane (right) directions. Lower panels: Dispersion of the high-energy plasmon $\omega_p(\mathbf{q})$ calculated along the in-plane (left) and out-of-plane (right) directions.

closely connected with the interlayer bonding. Moreover, the ratio of the out-of-plane and in-plane lattice constants c/a can be considered as a measure for the interlayer bonding strength in these systems [13, 39, 70]. In this regard, uniaxial strain applied in the out-of-plane direction is a promising way to tune the materials' properties. Inspired by recent experimental works, which indicate the possibility of a topological phase transition in nodal-line semimetals under external pressure [35, 70], here we study how the uniaxial strain would affect the optical properties of ZrSiS.

Before discussing the effect of strain on the electronic structure, we briefly focus on the mechanical properties of ZrSiS. We apply uniaxial strain in the direction perpendicular to the ZrSiS layers by varying the out-of-plane lattice constant c , and relaxing the in-plane lattice constant a . The calculated stress-strain curves are shown in Figure. 6. In case of uniaxial compressive strain along the out-of-plane direction (u_{zz}), the σ_{zz} vs. u_{zz} curve is nearly linear, indicating typical elastic regime and applicability of the Hooke's law. On the other hand, as can be seen from Figure. 6, the tensile strain is highly non-linear already at 2% tension. The observed nonlinearity of the elastic properties indicates a considerable modification of the electronic structure upon tensile strain. In Figure. 6, we also show the dependence of the in-plane strain u_{xx} with respect to u_{zz} . For u_{zz} in the range from -5% to $+5\%$, we obtain a perfect linear dependence, which allows us to estimate the Poisson's ratio. We ob-

tain $\nu = -du_{xx}/du_{zz} = 0.24$, which is in agreement with the results of previous studies [71].

Let us now discuss the strain-dependent electronic properties of ZrSiS. In Figure. 7(a), we show the band structures for the case of compressive and tensile uniaxial strain u_{zz} of 1%, 3%, and 5%. One can see that the linear dispersion of states near the Fermi energy is unaffected by the uniaxial strain in the range from -5% to $+5\%$. The position of the Dirac points near the Fermi energy changes slightly, which is not expected to have any noticeable effects on the optical transitions at low energies. On the other hand, the position of the nonsymmorphic Dirac node at the X and R points is more susceptible to strain. As has been pointed out by Andreas *et al.*, the location of these points in ZrSiX ($X = \text{S, Se, Te}$) correlates strongly with the chemical pressure c/a [13]. The most prominent effect of strain on the electronic structure of ZrSiS is the shift of the quadratic electron band along the energy axis. The tensile strain pushes this band toward the Fermi energy, while the compressive strain has the opposite effect. At around 2% tensile strain, the electron states along the Z-R line cross the Fermi energy. This behavior is expected to have influence on the optical properties in the low-energy region.

Upon uniaxial compression of ZrSiS, its Fermi surface does not undergo any considerable modification, remaining topologically equivalent to the Fermi surface of pristine ZrSiS shown in Figure. 1(c). In contrast, in case of tensile strain the Fermi surfaces changes its topol-

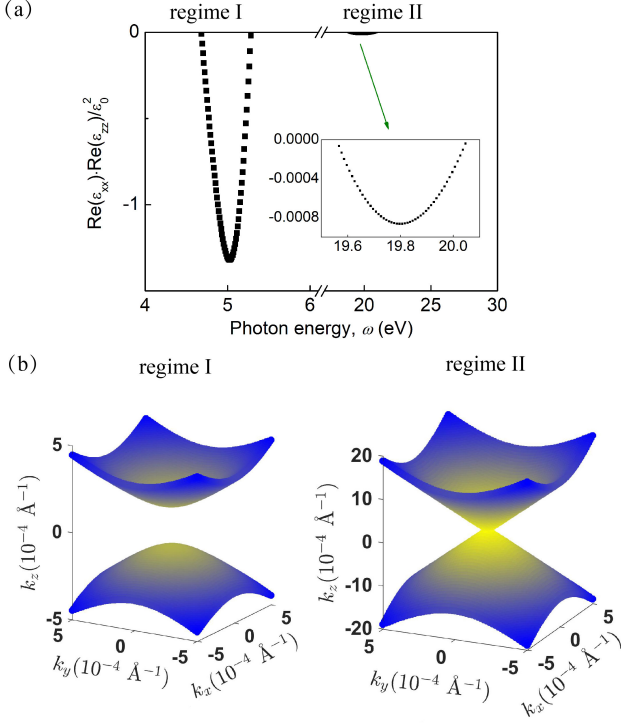


FIG. 5. (a) Product of the in-plane and out-plane real dielectric functions shown as a function of energy; (b) Reciprocal-space representation of the constant-energy surfaces of two possible hyperbolic plasmon modes in ZrSiS, denoted as regime I (left) and II (right). The color shows the magnitude of k_z .

ogy as a consequence of the emerged conduction states with quadratic dispersion. One can distinguish between two topological transitions occurring in stretched ZrSiS. When tensile stress reaches $P_1 \sim 1.3$ GPa, the previously disconnected hole pockets merge with each other, forming a ring at $k_z = \pi/c$. The corresponding merging region is highlighted in Figure 7(b). Up to 4% tension, the electron and hole pockets are connected along the Z–R direction. When tensile stress reaches $P_2 \sim 3.4$ GPa, a gap is being formed between the electron and hole pockets, manifesting itself the second transition in the Fermi surface topology [highlighted in Figure 7(b)].

We now examine the effect of strain on the interband screening. To this end, we first calculate the unscreened plasma frequency shown in Figure 8 for the two crystallographic directions. While out-of-plane plasma frequency $\omega_{p,zz}$ exhibits a pronounced linear dependence as a function of strain, the in-plane plasma frequency, $\omega_{p,xx}$ demonstrates a more sophisticated dependence. Different behavior of $\omega_{p,zz}$ and $\omega_{p,xx}$ can be attributed to the difference in the Fermi velocities along the x - and z - directions. The strain-dependent screened plasma frequency ω_p^{scr} can be obtained from $\epsilon_1(\omega)$ shown in Figure 9. For compressive strain and small tensile strain up to 2%, ω_p^{scr} remains nearly a constant of around 1.0 eV. The situation for larger tensile strain is different. Due to the electronic topological transitions, the nodal structure of

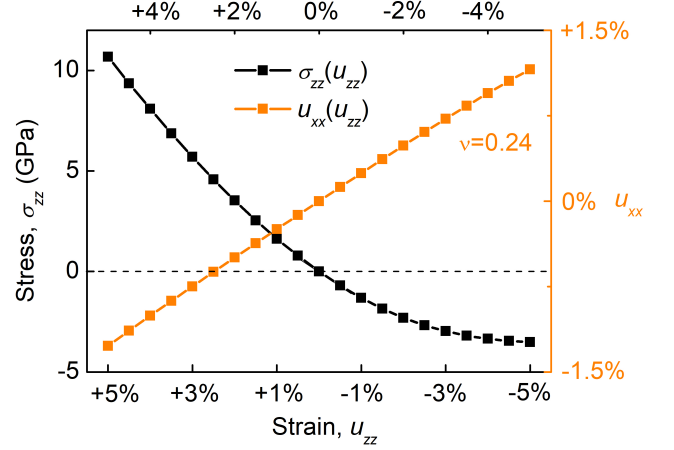


FIG. 6. Black curve: The zz -component of the stress tensor (σ_{zz}) as a function of the uniaxial strain u_{zz} in ZrSiS. Orange curve: In-plane strain u_{xx} versus out-of-plane strain u_{zz} . $\nu = -du_{xx}/du_{zz}$ is the corresponding Poisson ratio estimated by linear regression.

$\epsilon_1(\omega)$ changes, leading to an enhancement of ω_p^{scr} , which reaches ~ 1.3 eV at 4% tension. The related interband screening $\epsilon_\infty = (\omega_p/\omega_p^{scr})^2$ is changing accordingly. As it is shown in Figure 8, the in-plane component of ϵ_∞ is remaining around 9–10 up to 1% tension, after which it decreases rapidly until the tension reaches 4%, i.e. after the topological transition has occurred. In this regime, $\epsilon_\infty \sim 3$ –4, similar to the experimental values reported for ZrSiTe (~ 3.3) [70]. This result is in favor of the chemical pressure mechanism proposed to describe the difference between the ZrSiX ($X=S, Se, Te$) family members. Overall, the interband screening in moderately stretched ZrSiS is reduced considerably, which is expected to influence the optical response.

The in-plane conductivity calculated for different values and types of strain is shown in Figure 9 as a function of the photon energy. The frequency-independent conductivity region tends to narrow (broaden) as the compressive (tensile) strain is applied. Besides, the spectral weight in the low-energy region almost linearly enhances with pressure, gaining $\sim 50\%$ at 5% compression. On the contrary, the tensile strain reduces the spectral weight, yet not monotonously. At $\sim 3\%$ tension the optical conductivity is dropped, which apparently associated with the reduction of the interband contribution to the dielectric screening discussed earlier. The observed lowering of the spectral weight in stretched ZrSiS is in line with the smaller flat optical conductivity observed in ZrSiSe with a larger c/a lattice parameter [39].

At a larger energy scale, the effect of strain is less pronounced in the optical properties. In the range from 0.5 eV to 1.2 eV the optical conductivity is redshifted upon compression, while at larger frequencies it is blueshifted. The opposite situation is observed for the case of tensile strain. At low energies, the optical conductivity is mainly determined by the transitions between the linear

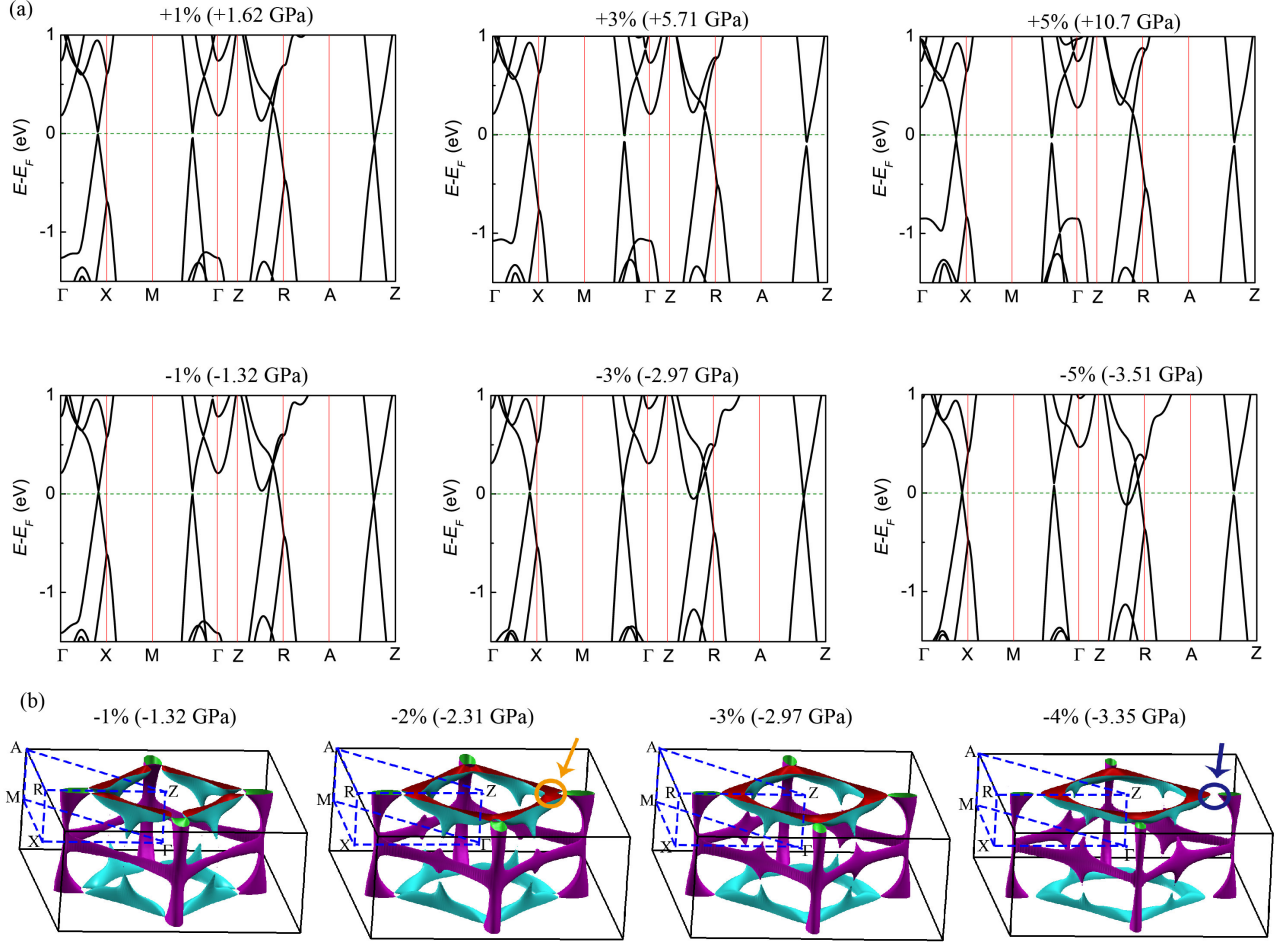


FIG. 7. (a) Band structures calculated in the vicinity of the Fermi energy for different values of the uniaxial strain u_{zz} in ZrSiS. Positive and negative values correspond to compression and tension, respectively. The related stress is given in parentheses; (b) The Fermi surfaces shown for the case of tensile strain, at which electronic topological transitions are taking place. Circles and arrows highlight the location where the transition occurs.

bands in the electronic structure, as well as by the details of the Fermi surface. At energies above 1 eV the transitions between the parabolic bands become important, whose position on the energy axis is largely dependent on strain. As a consequence, the characteristic U-shape of the optical conductivity around 1 eV almost disappears for more than 4% tensile strain.

Finally, we would like to comment on the effect of strain on the high-energy plasma excitations in ZrSiS. As this energy region is almost unrelated to the Fermi surface properties, the corresponding effect is less significant. In Figure. 10, we show the dispersion of the high-energy plasmon mode, as well as the corresponding parameters entering Eq.(10). Although the plasma frequency almost linearly changes with strain, the effect does not exceed a few percent for 5% strain. In contrast, the dispersion of the plasma excitations can be tuned effectively by the compressive strain. While the dispersion along the out-plane direction decreases with strain gaining 30% at +5%, the opposite effect is observed along the in-plane direction.

V. CONCLUSIONS

Based on first-principles calculations, we have systematically studied optical properties of nodal-line semimetal ZrSiS in the presence of uniaxial strain. We find that the characteristic frequency-independent optical conductivity is robust with respect to external pressure of up to 10 GPa. The compressive strain increases the spectral weight at low energies, but leads to a narrowing the flat conductivity region. The case of tensile strain is found to be more interesting. Upon tensile stress of 2 GPa, the Fermi surface undergoes a topological transition, resulting in a weakening of the interband dielectric screening. As a result, the spectral weight in the infrared region is reduced. The results obtained for stretched ZrSiS correlate with the properties of ZrSiSe and ZrSiTe, materials with larger lattice constants c/a . We, therefore, confirm the chemical pressure mechanism proposed in Ref. [39] to describe variability in the electronic and optical properties of the ZrSiX ($X=S, \text{Se}, \text{Te}$) family of compounds.

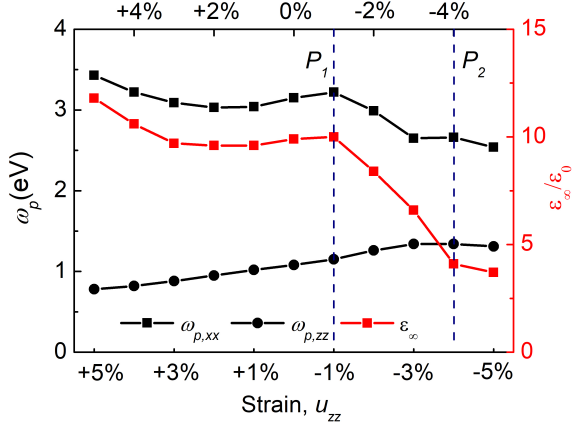


FIG. 8. Strain-dependent low-energy plasma frequency ω_p (black) estimated using Eq. (7) for in-plane and out-of-plane directions, and intraband screening constant $\epsilon_\infty = (\omega_{p,xx}/\omega_{p,xx}^{scr})^2$ (red) calculated for the in-plane direction shown as a function of the uniaxial strain. Positive and negative values correspond to compression and tension, respectively. $P_1 = -1.3$ GPa and $P_2 = -3.4$ GPa are the critical stress values around which the electronic topological transition takes place.

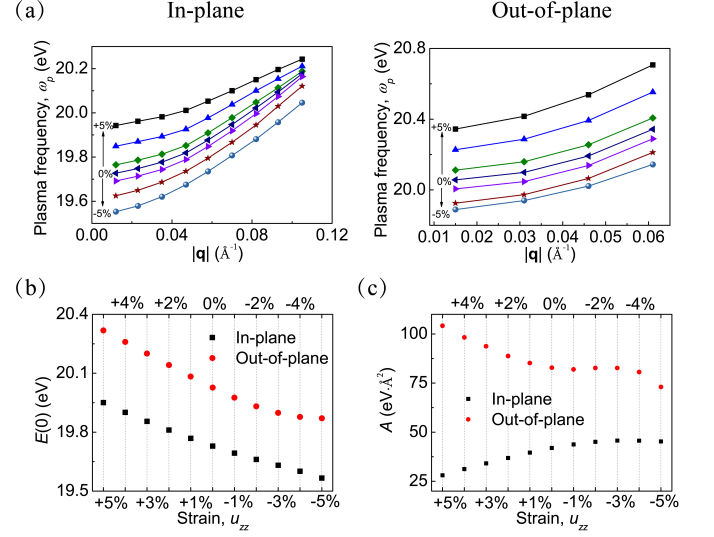


FIG. 10. (a) Plasma frequency ω_p as a function of momentum \mathbf{q} calculated for uniaxially strained ZrSiS along the in-plane (left) and out-of-plane (right) directions; (b) Plasma frequency in the long-wavelength limit ($\mathbf{q} \rightarrow 0$) [fitted with Eq. (10)] as a function of strain; (c) Plasmon dispersion [fitted with Eq. (10)] as a function of strain.

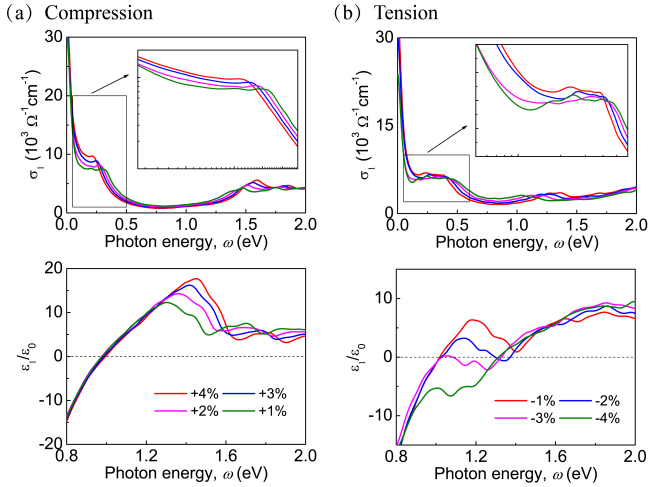


FIG. 9. Real part of the optical conductivity σ_1 (upper panels) and dielectric function ϵ_1 (lower panels) calculated for the in-plane direction under compressive (a) and tensile (b) strain as a function of the photon energy ω . The inset figures use logarithmic scale.

In the high-energy region, we found one lossy and one lossless plasmon modes at ~ 5 and ~ 20 eV, respectively. Although the frequencies of these modes remain almost unchanged in the presence of strain of up to 5%, their dispersion can be effectively tuned. Being a layered material, ZrSiS exhibits strongly anisotropic dielectric response between the in-layer and stacking directions. This gives rise to the possibility of existence of hyperbolic plasmons in ZrSiS. Our calculations show that the hyperbolic regime indeed may exist within a frequency

range of 0.6 eV around ~ 5 and ~ 20 eV. Overall, our findings provide insights into the mechanism behind the formation of optical properties in nodal-line semimetals ZrSiX, and pave the way for further optical studies, particularly in the ultraviolet spectral range.

ACKNOWLEDGMENTS

SY acknowledges financial support from the National Key R&D Program of China (Grant No. 2018FYA0305800) and National Science Foundation of

China (Grant No. 11774269). A.N.R. acknowledges travel support from FLAG-ERA JTC2017 Project GRANSFORT. Numerical calculations presented in this paper have been performed on a supercomputing system in the Supercomputing Center of Wuhan University.

-
- [1] D. J. Fisher, in *Topological Semimetals* (Materials Research Forum LLC, 2019).
- [2] S. M. Young, S. Zaheer, J. C. Y. Teo, C. L. Kane, E. J. Mele, and A. M. Rappe, *Dirac Semimetal in Three Dimensions*, *Phys. Rev. Lett.* **108**, 140405 (2012).
- [3] Z. Liu, B. Zhou, Y. Zhang, Z. Wang, H. Weng, D. Prabhakaran, S.-K. Mo, Z. Shen, Z. Fang, X. Dai, *et al.*, *Discovery of a three-dimensional topological Dirac semimetal, Na₃Bi*, *Science* **343**, 864 (2014).
- [4] B. Q. Lv, H. M. Weng, B. B. Fu, X. P. Wang, H. Miao, J. Ma, P. Richard, X. C. Huang, L. X. Zhao, G. F. Chen, Z. Fang, X. Dai, T. Qian, and H. Ding, *Experimental Discovery of Weyl Semimetal TaAs*, *Phys. Rev. X* **5**, 031013 (2015).
- [5] S.-Y. Xu, I. Belopolski, N. Alidoust, M. Neupane, G. Bian, C. Zhang, R. Sankar, G. Chang, Z. Yuan, C.-C. Lee, *et al.*, *Discovery of a Weyl fermion semimetal and topological Fermi arcs*, *Science* **349**, 613 (2015).
- [6] A. A. Burkov and L. Balents, *Weyl Semimetal in a Topological Insulator Multilayer*, *Phys. Rev. Lett.* **107**, 127205 (2011).
- [7] A. A. Burkov, M. D. Hook, and L. Balents, *Topological nodal semimetals*, *Phys. Rev. B* **84**, 235126 (2011).
- [8] R. Yu, H. Weng, Z. Fang, X. Dai, and X. Hu, *Topological Node-Line Semimetal and Dirac Semimetal State in Antiperovskite Cu₃PdN*, *Phys. Rev. Lett.* **115**, 036807 (2015).
- [9] Y. Chen, Y.-M. Lu, and H.-Y. Kee, *Topological crystalline metal in orthorhombic perovskite iridates*, *Nat. Commun.* **6**, 6593 (2015).
- [10] Y. Okamoto, T. Inohara, A. Yamakage, Y. Yamakawa, and K. Takenaka, *Low carrier density metal realized in candidate line-node Dirac semimetals CaAgP and CaAgAs*, *J. Phys. Soc. Jpn.* **85**, 123701 (2016).
- [11] G. Bian, T.-R. Chang, R. Sankar, S.-Y. Xu, H. Zheng, T. Neupert, C.-K. Chiu, S.-M. Huang, G. Chang, I. Belopolski, *et al.*, *Topological nodal-line fermions in spin-orbit metal PbTaSe₂*, *Nat. Commun.* **7**, 10556 (2016).
- [12] L. M. Schoop, M. N. Ali, C. Straßer, A. Topp, A. Varykhalov, D. Marchenko, V. Duppel, S. S. Parkin, B. V. Lotsch, and C. R. Ast, *Dirac cone protected by non-symmorphic symmetry and three-dimensional Dirac line node in ZrSiS*, *Nat. Commun.* **7**, 11696 (2016).
- [13] A. Topp, J. M. Lippmann, A. Varykhalov, V. Duppel, B. V. Lotsch, C. R. Ast, and L. M. Schoop, *Non-symmorphic band degeneracy at the Fermi level in ZrSiTe*, *New J. Phys.* **18**, 125014 (2016).
- [14] E. Emmanouilidou, B. Shen, X. Deng, T.-R. Chang, A. Shi, G. Kotliar, S.-Y. Xu, and N. Ni, *Magnetotransport properties of the single-crystalline nodal-line semimetal candidates CaTX (T = Ag, Cd; X = As, Ge)*, *Phys. Rev. B* **95**, 245113 (2017).
- [15] M. Matusiak, J. Cooper, and D. Kaczorowski, *Thermoelectric quantum oscillations in ZrSiS*, *Nat. Commun.* **8**, 15219 (2017).
- [16] J. Hu, Z. Tang, J. Liu, X. Liu, Y. Zhu, D. Graf, K. Myhro, S. Tran, C. N. Lau, J. Wei, and Z. Mao, *Evidence of Topological Nodal-Line Fermions in ZrSiSe and ZrSiTe*, *Phys. Rev. Lett.* **117**, 016602 (2016).
- [17] M. M. Hosen, K. Dimitri, I. Belopolski, P. Maldonado, R. Sankar, N. Dhakal, G. Dhakal, T. Cole, P. M. Oppeneer, D. Kaczorowski, F. Chou, M. Z. Hasan, T. Durakiewicz, and M. Neupane, *Tunability of the topological nodal-line semimetal phase in ZrSiX-type materials (X = S, Se, Te)*, *Phys. Rev. B* **95**, 161101 (2017).
- [18] A. Topp, R. Queiroz, A. Grüneis, L. Mühler, A. W. Rost, A. Varykhalov, D. Marchenko, M. Krivenkov, F. Rodolakis, J. L. McChesney, B. V. Lotsch, L. M. Schoop, and C. R. Ast, *Surface Floating 2D Bands in Layered Nonsymmorphic Semimetals: ZrSiS and Related Compounds*, *Phys. Rev. X* **7**, 041073 (2017).
- [19] C. Chen, X. Xu, J. Jiang, S.-C. Wu, Y. P. Qi, L. X. Yang, M. X. Wang, Y. Sun, N. B. M. Schröter, H. F. Yang, L. M. Schoop, Y. Y. Lv, J. Zhou, Y. B. Chen, S. H. Yao, M. H. Lu, Y. F. Chen, C. Felser, B. H. Yan, Z. K. Liu, and Y. L. Chen, *Dirac line nodes and effect of spin-orbit coupling in the nonsymmorphic critical semimetals MSiS (M=Hf,Zr)*, *Phys. Rev. B* **95**, 125126 (2017).
- [20] B. Fu, C. Yi, T. Zhang, M. Caputo, J. Ma, X. Gao, B. Lv, L. Kong, Y. Huang, M. Shi, *et al.*, *arXiv preprint arXiv:1712.00782* (2017).
- [21] C. J. Butler, Y.-M. Wu, C.-R. Hsing, Y. Tseng, R. Sankar, C.-M. Wei, F.-C. Chou, and M.-T. Lin, *Quasiparticle interference in ZrSiS: Strongly band-selective scattering depending on impurity lattice site*, *Phys. Rev. B* **96**, 195125 (2017).
- [22] M. S. Lodge, G. Chang, C.-Y. Huang, B. Singh, J. Hellertedt, M. T. Edmonds, D. Kaczorowski, M. M. Hosen, M. Neupane, H. Lin, *et al.*, *Observation of effective pseudospin scattering in ZrSiS*, *Nano Lett.* **17**, 7213 (2017).
- [23] S. Pezzini, M. Van Delft, L. Schoop, B. Lotsch, A. Carrington, M. Katsnelson, N. Hussey, and S. Wiedmann, *Unconventional mass enhancement around the Dirac nodal loop in ZrSiS*, *Nat. Phys.* **14**, 178 (2018).
- [24] J. Hu, Z. Tang, J. Liu, Y. Zhu, J. Wei, and Z. Mao, *Nearly massless Dirac fermions and strong Zeeman splitting in the nodal-line semimetal ZrSiS probed by de Haas-van Alphen quantum oscillations*, *Phys. Rev. B* **96**, 045127 (2017).
- [25] X. Wang, X. Pan, M. Gao, J. Yu, J. Jiang, J. Zhang, H. Zuo, M. Zhang, Z. Wei, W. Niu, *et al.*, *Evidence of both surface and bulk Dirac bands and anisotropic nonsaturating magnetoresistance in ZrSiS*, *Adv. Electron. Mater.* **2**, 1600228 (2016).
- [26] R. Singha, A. K. Pariari, B. Satpati, and P. Mandal, *Large nonsaturating magnetoresistance and signature of nondegenerate Dirac nodes in ZrSiS*, *Proc. Natl. Acad. Sci.* **114**, 2468 (2017).
- [27] M. N. Ali, L. M. Schoop, C. Garg, J. M. Lippmann, E. Lara, B. Lotsch, and S. S. Parkin, *Butterfly mag-*

- netoresistance, quasi-2D Dirac Fermi surface and topological phase transition in ZrSiS, *Sci. Adv.* **2**, e1601742 (2016).
- [28] H. Pan, B. Tong, J. Yu, J. Wang, D. Fu, S. Zhang, B. Wu, X. Wan, C. Zhang, X. Wang, *et al.*, Three-dimensional anisotropic magnetoresistance in the Dirac node-line material ZrSiSe, *Sci. Rep.* **8**, 9340 (2018).
- [29] R. Sankar, G. Peramaiyan, I. P. Muthuselvam, C. J. Butler, K. Dimitri, M. Neupane, G. N. Rao, M.-T. Lin, and F. Chou, Crystal growth of Dirac semimetal ZrSiS with high magnetoresistance and mobility, *Sci. Rep.* **7**, 40603 (2017).
- [30] R. Lam and A. Mar, New Ternary Zirconium Antimonides, $ZrSi_{0.7}Sb_{1.3}$, $ZrGeSb$, and $ZrSn_{0.4}Sb_{1.6}$: A Family Containing ZrSiS-Type and β -ZrSb₂-Type Compounds, *J. Solid State Chem.* **134**, 388 (1997).
- [31] M. Neupane, I. Belopolski, M. M. Hosen, D. S. Sanchez, R. Sankar, M. Szlowska, S.-Y. Xu, K. Dimitri, N. Dhakal, P. Maldonado, P. M. Oppeneer, D. Kaczorowski, F. Chou, M. Z. Hasan, and T. Durakiewicz, Observation of topological nodal fermion semimetal phase in ZrSiS, *Phys. Rev. B* **93**, 201104 (2016).
- [32] M. B. Schilling, L. M. Schoop, B. V. Lotsch, M. Dressel, and A. V. Pronin, Flat Optical Conductivity in ZrSiS due to Two-Dimensional Dirac Bands, *Phys. Rev. Lett.* **119**, 187401 (2017).
- [33] A. N. Rudenko, E. A. Stepanov, A. I. Lichtenstein, and M. I. Katsnelson, Excitonic Instability and Pseudogap Formation in Nodal Line Semimetal ZrSiS, *Phys. Rev. Lett.* **120**, 216401 (2018).
- [34] M. M. Scherer, C. Honerkamp, A. N. Rudenko, E. A. Stepanov, A. I. Lichtenstein, and M. I. Katsnelson, Excitonic instability and unconventional pairing in the nodal-line materials ZrSiS and ZrSiSe, *Phys. Rev. B* **98**, 241112 (2018).
- [35] D. VanGennep, T. A. Paul, C. W. Yergler, S. T. Weir, Y. K. Vohra, and J. J. Hamlin, Possible pressure-induced topological quantum phase transition in the nodal line semimetal ZrSiS, *Phys. Rev. B* **99**, 085204 (2019).
- [36] A. B. Kuzmenko, E. van Heumen, F. Carbone, and D. van der Marel, Universal Optical Conductance of Graphite, *Phys. Rev. Lett.* **100**, 117401 (2008).
- [37] K. F. Mak, M. Y. Sfeir, Y. Wu, C. H. Lui, J. A. Misewich, and T. F. Heinz, Measurement of the Optical Conductivity of Graphene, *Phys. Rev. Lett.* **101**, 196405 (2008).
- [38] T. Habe and M. Koshino, Dynamical conductivity in the topological nodal-line semimetal ZrSiS, *Phys. Rev. B* **98**, 125201 (2018).
- [39] J. Ebad-Allah, J. F. Afonso, M. Krottenmüller, J. Hu, Y. L. Zhu, Z. Q. Mao, J. Kuneš, and C. A. Kuntscher, Chemical pressure effect on the optical conductivity of the nodal-line semimetals ZrSiY ($Y = S, Se, Te$) and ZrGeY ($Y = S, Te$), *Phys. Rev. B* **99**, 125154 (2019).
- [40] Y.-Y. Lv, B.-B. Zhang, X. Li, S.-H. Yao, Y. Chen, J. Zhou, S.-T. Zhang, M.-H. Lu, and Y.-F. Chen, Extremely large and significantly anisotropic magnetoresistance in ZrSiS single crystals, *Appl. Phys. Lett.* **108**, 244101 (2016).
- [41] A. Politano and G. Chiarello, The influence of electron confinement, quantum size effects, and film morphology on the dispersion and the damping of plasmonic modes in Ag and Au thin films, *Progr. Surf. Sci.* **90**, 144 (2015).
- [42] J. M. McMahon, G. C. Schatz, and S. K. Gray, Plasmonics in the ultraviolet with the poor metals Al, Ga, In, Sn, Tl, Pb, and Bi, *Phys. Chem. Chem. Phys.* **15**, 5415 (2013).
- [43] A. Taguchi, Y. Saito, K. Watanabe, S. Yijian, and S. Kawata, Tailoring plasmon resonances in the deep-ultraviolet by size-tunable fabrication of aluminum nanostructures, *Appl. Phys. Lett.* **101**, 081110 (2012).
- [44] S. C. Dhanabalan, J. S. Ponraj, H. Zhang, and Q. Bao, Present perspectives of broadband photodetectors based on nanobelts, nanoribbons, nanosheets and the emerging 2D materials, *Nanoscale* **8**, 6410 (2016).
- [45] X. Zhang, K. Wang, J. Ma, Q. Zhang, P. Yan, and X. Tian, Ultraviolet Imaging Based on Surface Plasmon Resonance With Azo-Polymer Sensing Layer, *IEEE Photonics Technol. Lett.* **27**, 1297 (2015).
- [46] S.-I. Nakashima, H. Okumura, T. Yamamoto, and R. Shimidzu, Deep-ultraviolet Raman microspectroscopy: characterization of wide-gap semiconductors, *Appl. Spectrosc.* **58**, 224 (2004).
- [47] M. K. Hedayati, A. Zillohu, T. Strunskus, F. Faupel, and M. Elbahri, Plasmonic tunable metamaterial absorber as ultraviolet protection film, *Appl. Phys. Lett.* **104**, 041103 (2014).
- [48] P. Giannozzi, O. Andreussi, T. Brumme, O. Bunau, M. B. Nardelli, M. Calandra, R. Car, C. Cavazzoni, D. Ceresoli, M. Cococcioni, *et al.*, Advanced capabilities for materials modelling with Quantum ESPRESSO, *J. Phys. Condens. Matter* **29**, 465901 (2017).
- [49] J. P. Perdew, K. Burke, and M. Ernzerhof, Generalized Gradient Approximation Made Simple, *Phys. Rev. Lett.* **77**, 3865 (1996).
- [50] D. R. Hamann, M. Schlüter, and C. Chiang, Norm-Conserving Pseudopotentials, *Phys. Rev. Lett.* **43**, 1494 (1979).
- [51] A. Kokalj, Computer graphics and graphical user interfaces as tools in simulations of matter at the atomic scale, *Comp. Mater. Sci.* **28**, 155 (2003).
- [52] A. Marini, C. Hogan, M. Grüning, and D. Varsano, Yambo: an *ab initio* tool for excited state calculations, *Comp. Phys. Commun.* **180**, 1392 (2009).
- [53] G. Onida, L. Reining, and A. Rubio, Electronic excitations: density-functional versus many-body Green's-function approaches, *Rev. Mod. Phys.* **74**, 601 (2002).
- [54] M. P. Marder, *Condensed matter physics* (John Wiley & Sons, 2010).
- [55] D. Sangalli, A. Ferretti, H. Miranda, C. Attaccalite, I. Marri, E. Cannuccia, P. Melo, M. Marsili, F. Paleari, A. Marrazzo, *et al.*, Many-body perturbation theory calculations using the yambo code, *J. Phys.: Cond. Matter* **31**, 325902 (2019).
- [56] M. Dressel and G. Grüner, *Electrodynamics of Solids* Cambridge University Press, Cambridge, UK (2002).
- [57] K.-H. Lee and K. J. Chang, First-principles study of the optical properties and the dielectric response of Al, *Phys. Rev. B* **49**, 2362 (1994).
- [58] J. Harl, G. Kresse, L. D. Sun, M. Hohage, and P. Zeppenfeld, *Ab initio* reflectance difference spectra of the bare and adsorbate covered Cu(110) surfaces, *Phys. Rev. B* **76**, 035436 (2007).
- [59] G. Prandini, M. Galante, N. Marzari, and P. Umari, SIMPLE code: optical properties with optimal basis functions, *Comp. Phys. Commun.* (2019).
- [60] G. Nicotra, E. van Veen, I. Deretzis, L. Wang, J. Hu, Z. Mao, V. Fabio, C. Spinella, G. Chiarello, A. Rudenko, *et al.*, Anisotropic ultraviolet-plasmon dispersion in black phosphorus, *Nanoscale* **10**, 21918 (2018).
- [61] L. Sang, M. Liao, and M. Sumiya, A comprehensive

- review of semiconductor ultraviolet photodetectors: from thin film to one-dimensional nanostructures*, *Sensors* **13**, 10482 (2013).
- [62] P. Shekhar, J. Atkinson, and Z. Jacob, *Hyperbolic metamaterials: fundamentals and applications*, *Nano Converg.* **1**, 14 (2014).
- [63] J. S. Gomez-Diaz, M. Tymchenko, and A. Alù, *Hyperbolic Plasmons and Topological Transitions Over Uniaxial Metasurfaces*, *Phys. Rev. Lett.* **114**, 233901 (2015).
- [64] M. N. Gjerding, R. Petersen, T. G. Pedersen, N. A. Mortensen, and K. S. Thygesen, *Layered van der Waals crystals with hyperbolic light dispersion*, *Nat. Commun.* **8**, 320 (2017).
- [65] Y. Guo, W. Newman, C. L. Cortes, and Z. Jacob, *Applications of hyperbolic metamaterial substrates*, *Adv. Optoelectron.* **2012**, 452502 (2012).
- [66] J. Yao, Z. Liu, Y. Liu, Y. Wang, C. Sun, G. Bartal, A. M. Stacy, and X. Zhang, *Optical negative refraction in bulk metamaterials of nanowires*, *Science* **321**, 930 (2008).
- [67] A. J. Hoffman, L. Alekseyev, S. S. Howard, K. J. Franz, D. Wasserman, V. A. Podolskiy, E. E. Narimanov, D. L. Sivco, and C. Gmachl, *Negative refraction in semiconductor metamaterials*, *Nat. Mater.* **6**, 946 (2007).
- [68] P. V. Kapitanova, P. Ginzburg, F. J. Rodríguez-Fortuño, D. S. Filonov, P. M. Voroshilov, P. A. Belov, A. N. Poddubny, Y. S. Kivshar, G. A. Wurtz, and A. V. Zayats, *Photonic spin Hall effect in hyperbolic metamaterials for polarization-controlled routing of subwavelength modes*, *Nat. Commun.* **5**, 3226 (2014).
- [69] S.-A. Biehs, M. Tschikin, and P. Ben-Abdallah, *Hyperbolic Metamaterials as an Analog of a Blackbody in the Near Field*, *Phys. Rev. Lett.* **109**, 104301 (2012).
- [70] J. Ebad-Allah, M. Krottenmüller, J. Hu, Y. L. Zhu, Z. Q. Mao, and C. A. Kuntscher, *Infrared spectroscopy study of the nodal-line semimetal candidate ZrSiTe under pressure: Hints for pressure-induced phase transitions*, *Phys. Rev. B* **99**, 245133 (2019).
- [71] B. Salmankurt and S. Duman, *First-principles study of structural, mechanical, lattice dynamical and thermal properties of nodal-line semimetals ZrXY ($X=Si, Ge$; $Y=S, Se$)*, *Philos. Mag.* **97**, 175 (2017).